

---

# RadSplatter: Extending 3D Gaussian Splatting to Radio Frequencies for Wireless Radiomap Extrapolation

---

Yiheng Wang<sup>1,2</sup> Ye Xue<sup>1,2</sup> Shutao Zhang<sup>1,3</sup> Tsung-Hui Chang<sup>1,3</sup>

## Abstract

A radiomap represents the spatial distribution of wireless signal strength, critical for applications like network optimization and autonomous driving. However, constructing radiomap relies on measuring radio signal power across the entire system, which is costly in outdoor environments due to large network scales. We present RadSplatter, a framework that extends 3D Gaussian Splatting (3DGS) to radio frequencies for efficient and accurate radiomap extrapolation from sparse measurements. RadSplatter models environmental scatterers and radio paths using 3D Gaussians, capturing key factors of radio wave propagation. It employs a relaxed-mean (RM) scheme to reparameterize the positions of 3D Gaussians from noisy and dense 3D point clouds. A camera-free 3DGS-based projection is proposed to map 3D Gaussians onto 2D radio beam patterns. Furthermore, a regularized loss function and recursive fine-tuning using highly structured sparse measurements in real-world settings are applied to ensure robust generalization. Experiments on synthetic and real-world data show state-of-the-art extrapolation accuracy and execution speed.

## 1. Introduction

In recent years, 3D Gaussian Splatting (3DGS) (Kerbl et al., 2023) and 3D environment representation (Rusu & Cousins, 2011) have gained significant attention in computer vision and graphics, leading to numerous advancements. For example, Zhou et al. (2024b) extended 3DGS for reconstructing dynamic scenes in autonomous driving, leveraging LiDAR point cloud data. Li et al. (2024) introduced depth regu-

larization to facilitate few-shot novel view synthesis, while another study (Fu et al., 2024) achieved novel view synthesis without pre-computed camera poses. However, these works focus primarily on visible light applications. In contrast, our work firstly extends 3DGS to the radio frequency domain, addressing challenges in modeling wireless signal radiation.

Radiomaps, which represent the spatial distribution of wireless signal strength, are critical for applications such as *network optimization*, *resource allocation*, and *autonomous driving*. However, constructing radiomaps with dense signal strength measurements is highly impractical, particularly in outdoor environments. Signal strength data is typically sparse, as it is collected manually through labor-intensive methods such as drive tests, where engineers traverse coverage areas with specialized equipment to sample wireless signals at specific locations. This process is costly and limited in scope, resulting in incomplete radiomaps. Moreover, outdoor environments are vast and complex, and wireless signals are influenced by obstacles, interference, and environmental conditions, making robust and efficient radiomap reconstruction methods essential.

Traditional approaches for radiomap reconstruction, such as *inverse distance weighting (IDW)* (Kuo & Tseng, 2010) and *Kriging* (Sato et al., 2020), rely on fixed-function models to interpolate missing data. While computationally efficient, these methods struggle to handle the complexity of outdoor environments and fail to capture the underlying physics of wireless signal propagation. *Ray-tracing* (Bi et al., 2019) methods simulate wireless signal paths using computer-aided design (CAD) representations of environments, but such models often fail to adapt to real-world scenarios due to discrepancies between modeled and actual environments. Learning-based methods, such as *variational autoencoders (VAE)* (Teganya & Romero, 2021) and *deep convolutional GANs (DCGAN)* (Radford, 2015), offer a data-driven alternative by avoiding explicit assumptions about signal propagation. However, these approaches require dense measurements for effective training and fail to incorporate the physics of wireless signals, limiting their utility in sparse, real-world settings. Recent NeRF-based approaches (Mildenhall et al., 2021), including NeWRF (Lu et al., 2024), have demonstrated potential in radiomap recon-

---

\*Equal contribution <sup>1</sup>Shenzhen Research Institute of Big Data, Shenzhen, China <sup>2</sup>School of Data Science, The Chinese University of Hong Kong-Shenzhen, Shenzhen, China <sup>3</sup>School of Science and Engineering, The Chinese University of Hong Kong-Shenzhen, Shenzhen, China. Correspondence to: Ye Xue <yexue@cuhk.edu.cn>.

struction but suffer from high computational complexity and slow synthesis speeds, making them unsuitable for large-scale outdoor environments.

In contrast, *3D Gaussian Splatting-based models* are computationally efficient and align well with wireless signal propagation characteristics. Their anisotropic 3D Gaussian volumetric representation is particularly suited to modeling scatterers in the environment that influence signal behavior. Furthermore, LiDAR point clouds—providing accurate representations of outdoor environments (Villani et al., 2018)—can be directly utilized to initialize 3DGS, enabling these models to effectively capture interactions between signals and the environment (Sun et al., 2023). However, applying 3DGS to radiomap reconstruction presents unique challenges. First, processing dense point cloud data in large-scale outdoor areas incurs significant computational costs (Mi et al., 2024). Second, traditional 3DGS relies on camera-based calibration to map 3D world coordinates to 2D projections, which is infeasible for wireless signals. Finally, sparse signal strength measurements lack sufficient data for accurate extrapolation in uncovered regions, making robust generalization a critical challenge.

To address these challenges, we propose *RadSplatter*, a framework that extends 3D Gaussian Splatting to the radio frequency domain for efficient and accurate radiomap reconstruction. Our contributions are summarized as follows:

- **Relaxed-Mean reparameterization:** We propose a novel RM scheme to select key virtual scatterers from noisy and dense point clouds, providing an accurate reparameterization of means for radio 3D Gaussians. These novel trainable parameters in RM are jointly optimized with the whole model’s other parameters, enabling efficient gradient-based training.
- **Camera-free 3DGS framework:** We introduce the first camera-free 3DGS-based framework for wireless signal strength reconstruction, integrating radio multipath propagation characteristics and environmental semantics. This framework learns wireless radiation patterns from sparse signal strength measurements within milliseconds, even in complex outdoor environments.
- **Extrapolation-enhancing techniques:** To improve extrapolation performance, we propose a ternary regularized loss function and a recursive fine-tuning scheme. The fine-tuning process leverages predicted data to iteratively refine the model for improved accuracy in regions with sparse or no measurements.

## 2. Preliminaries

In this section, we present preliminaries on 3D Gaussian Splatting and wireless signal propagation, focusing on how

signal strength is collected and the challenges of radiomap reconstruction.

### 2.1. 3D Gaussian Splatting (3DGS)

3DGS (Kerbl et al., 2023) is an explicit radiance field-based scene representation that models a radiance field using a large number of total  $I$  3D anisotropic balls, the  $i$ -th 3D Gaussian is defined as:

$$G_i(\mathbf{x}) = e^{-\frac{1}{2}(\mathbf{x}-\boldsymbol{\mu}_i)^T \boldsymbol{\Sigma}_i^{-1}(\mathbf{x}-\boldsymbol{\mu}_i)}, \quad (1)$$

where  $\mathbf{x} = (x_0, x_1, x_2)$  denotes the three-dimensional spatial coordinates of the Gaussian point and  $\boldsymbol{\mu}_i \in \mathbb{R}^3$  and  $\boldsymbol{\Sigma}_i \in \mathbb{R}^{3 \times 3}$  denote the mean and variance of the Gaussian representation.<sup>1</sup> Besides, the  $i$ -th anisotropic ball is also characterized by parameters that include its opacity  $\alpha_i \in \mathbb{R}$  and the Spherical Harmonics (SH) coefficients  $\boldsymbol{\tau}_i \in \mathbb{R}^{3 \times (k+1)^2}$  (where  $k$  is the degree of the SH function  $\mathbf{sh}(\cdot, k)$ ) (Fridovich-Keil et al., 2022) for modeling view-dependent color. Specifically, the color of the  $i$ -th 3D Gaussian at the view direction  $\mathbf{v}_i$  is

$$\mathbf{c}_i = \mathbf{sh}(\boldsymbol{\tau}_i, \mathbf{v}_i, k) \in \mathbb{R}^3. \quad (2)$$

During the rendering phase, the 3D Gaussians  $\{G_i(\mathbf{x})\}_{i=1}^I$  are projected (rasterized) onto the image plane, forming 2D Gaussian splats, which can be expressed as  $\{\mathbf{w}_i(\mathbf{p}) = \text{Proj}_{\text{EWA}}(G_i(\mathbf{x}))\}_{i=1}^I$  at the  $\mathbf{p}$ -th pixel, as described in (Zwicker et al., 2002). The 2D Gaussian splats are sorted from front to back tile-wisely, and *alpha*-blending algorithm is applied to approximate the  $\mathbf{p}$ -th pixel RGB value  $\mathbf{C}(\mathbf{p}) \in \mathbb{R}^3$  as

$$\mathbf{C}(\mathbf{p}) = \sum_{i \in \mathbb{I}_p} \mathbf{c}_i \alpha_i \cdot \mathbf{w}_i(\mathbf{p}) \prod_{j=1}^{i-1} (1 - \alpha_j \cdot \mathbf{w}_j(\mathbf{p})), \quad (3)$$

where  $\mathbb{I}_p$  is the set of splats that contribute to the  $\mathbf{p}$ -th pixel. After computing the color for each pixel, the rendered image is compared to the ground-truth image to calculate the pixel-wise loss. This loss is then used to update the model’s properties parameters  $\boldsymbol{\Phi} = \{(\boldsymbol{\mu}_i, \boldsymbol{\Sigma}_i, \alpha_i, \boldsymbol{\tau}_i), i \in [I]\}$ , ensuring the rendered scene aligns closely with the target, where  $[I]$  denotes the vector consisting of  $[1, \dots, I]$ .

### 2.2. Radio Signal Propagation Mechanism

Radiomaps are 2D representations of the spatial distribution of *Received Signal Power* (RSS), which quantifies the

<sup>1</sup>The covariance matrix  $\boldsymbol{\Sigma}_i$ , which defines the ellipsoid shape of the  $i$ -th Gaussian, can be expressed in terms of a scaling matrix  $\mathbf{S}_i \in \mathbb{R}^{3 \times 3}$  and a rotation matrix  $\mathbf{R}_i \in \mathbb{R}^{3 \times 3}$  using its Eigen-Composition. Here, the rotation matrix  $\mathbf{R}_i$  is parameterized using quaternions  $\mathbf{r}_i \in \mathbb{R}^4$ , while the scaling factors are represented by  $\mathbf{s}_i \in \mathbb{R}^3$ .

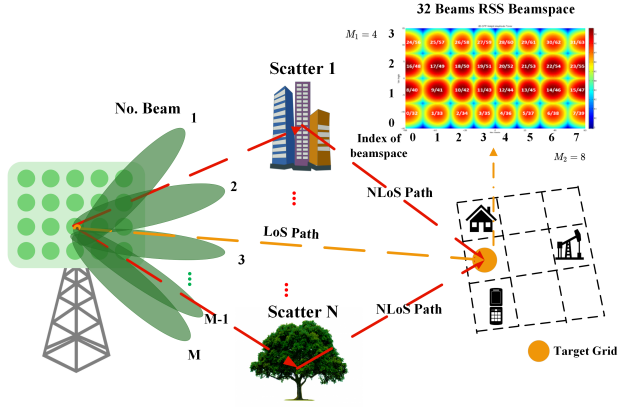


Figure 1. Illustration of wireless communication setup and RSS beamspace. The orange line represents the LoS channel path, while the red line shows the NLoS path.

power of wireless signals across a region. In modern wireless communication systems, RSS is often measured in the *beamspace*, where predefined beams divide the coverage space into angular regions, as shown in Figure 1, the coverage space is divided by  $M = M_1 \times M_2$  beams. For the  $m$ -th beam at the  $l$ -th location, the RSS can be computed as

$$RSS_{m,l} = P|h_{m,l}|^2, \quad (4)$$

where  $P$  is the transmission power, and  $h_{m,l}$  represents the wireless channel, which characterizes the effects of the propagation process, including signal attenuation and phase changes.

Wireless signal propagation is influenced by both a direct line-of-sight (LoS) path and multiple non-line-of-sight (NLoS) paths caused by environmental scatterers such as buildings and walls. These scatterers induce phenomena such as reflection, diffraction, and scattering (Kapusuz & Kara, 2014), resulting in a phenomenon known as *multi-path propagation* (Bertoni, 1999). Multi-path propagation significantly impacts RSS, as the received signal is the superposition of multiple propagation paths, each contributing distinct attenuation and phase changes. The wireless channel, which encapsulates the impact of the propagation process at location  $l$ , aggregating all  $M$  beams, can be expressed as

$$h_l = \sum_{n=1}^N \Delta\beta_n \odot e^{j\Delta\varphi_n}, \quad (5)$$

where  $N$  is the total number of paths caused by  $N$  scatters<sup>2</sup>,  $\Delta\beta_n \in \mathbb{R}^M$  denotes the attenuation of the signal strength, and  $\Delta\varphi_n \in \mathbb{R}^M$  represents the phase shift contributed by the  $n$ -th path.  $\odot$  denotes the Hadamard product.

<sup>2</sup>Here we assume each scatter induces one radio propagation path for simplicity

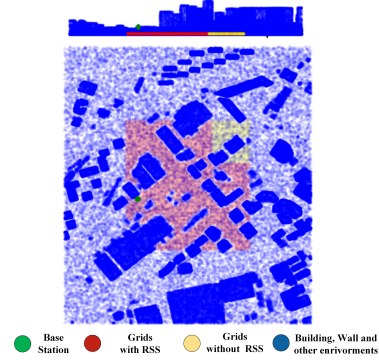


Figure 2. Illustration of the Front and Top Views of a 3D Point Cloud of Shanghai's Outdoor Environment.

The inherent complexity of multi-path propagation, combined with the variability of wireless environments, poses significant challenges for constructing accurate radiomaps. Sparse RSS measurements further exacerbate these difficulties, as manual field surveys (e.g., drive tests) are labor-intensive and costly, leaving large terrain areas under-sampled. These limitations lead to incomplete or low-resolution radiomaps, which fail to capture the intricate spatial variations in signal power caused by environmental factors.

### 3. RadSplatter

In this section, we present RadSplatter, a novel framework designed to extend 3DGS to the radio frequency domain for RSS radiomap extrapolation in outdoor environments.

#### 3.1. Problem Description and Framework Overview

Radiomap extrapolation in large-scale outdoor environments is challenging due to sparse and incomplete RSS measurements, which are typically collected only in limited regions (red grids  $\mathbb{L}_k$  in Figure 2). This leaves large areas (yellow grids  $\mathbb{L}_o$ ) without coverage, necessitating a method to predict RSS values in these unseen regions. To address this, RadSplatter leverages sparse RSS data, the base station (BS) position, and environmental features, such as buildings and walls that strongly influence wireless signal propagation through reflection, scattering, and diffraction. However, obtaining such environmental features is infeasible in classical wireless measurement campaigns, as no scene details can be captured. Thanks to advancements in Integrated Sensing and Communication (ISAC), modern wireless measurement campaigns can now collect 3D point clouds alongside RSS data. These point clouds provide detailed geometric representations of the environment, enabling models to account for the spatial structure of obstacles that impact signal behavior.

In this work, we propose **RadSplatter**, a novel framework that extends 3DGS to the radio frequency domain. RadSplatter leverages sparse RSS data, the position of BS, and environmental features derived from 3D point clouds to predict RSS values in complex, unseen locations.  $N$  radio scatterers, such as buildings and walls, are represented using anisotropic 3D Gaussians, which capture their signal-related properties. These scatterers serve as the foundation for modeling signal propagation paths, and their characteristics are described as **RadSplatter attributes**:

$$\Phi_{\text{rad}} \triangleq \{(\boldsymbol{\mu}_n^{\text{rad}}, \boldsymbol{\Sigma}_n^{\text{rad}}, \boldsymbol{\alpha}_n^{\text{rad}}, \boldsymbol{\tau}_n^{\text{rad}})\}_{n=1}^N, \quad (6)$$

where  $\boldsymbol{\mu}_n^{\text{rad}}$  is the scatterer position representing the spatial locations of the  $n$ -th scatterer,  $\boldsymbol{\alpha}_n^{\text{rad}}$  is the signal attenuation reflecting both the magnitude attenuation and phase change of the radio signal caused by the  $n$ -th scatterer,  $\boldsymbol{\Sigma}_n^{\text{rad}}$  is the covariance matrix that defines the anisotropic spatial uncertainty of the  $n$ -th scatterer, and  $\boldsymbol{\tau}_n^{\text{rad}}$  is the RSS-encoded spherical harmonics coefficients capturing how the scatterer's contribution changes with respect to the direction of the signal propagation.

Specifically, RadSplatter predicts RSS values  $\{\hat{y}_l \in \mathbb{R}^M\}$  for target locations  $P_l \in \mathbb{R}^3$  given the BS position  $P_{\text{BS}} \in \mathbb{R}^3$ . This mapping is achieved using the RadSplatter attributes, collectively denoted as  $\Phi_{\text{rad}}$ . The prediction process is mathematically formalized as:

$$\mathcal{F}_{\Phi_{\text{rad}}} : (P_{\text{BS}}, P_l) \rightarrow \hat{y}_l. \quad (7)$$

To facilitate this process, RadSplatter employs a preprocessing model  $G$  that extracts key environmental information from dense and noisy 3D point clouds. Specifically,  $G$  identifies the positions of the key scatterers  $\{\boldsymbol{\mu}_n^{\text{rad}}\}_{n=1}^N$ , which form one of the critical RadSplatter attributes in  $\Phi_{\text{rad}}$ . These scatterer positions are essential for modeling the effects of signal propagation. However, identifying relevant scatterers from raw point clouds remains a significant challenge. To address this, RadSplatter incorporates an optimization-based preprocessing method, referred to as the **relaxed-mean (RM) scheme**, which reparameterizes the positions of the 3D Gaussians. Given the raw point cloud data  $\hat{P}_{\text{raw}} \in \mathbb{R}^{R \times 3}$ , consisting of  $R$  points, and the BS position  $P_{\text{BS}} \in \mathbb{R}^3$ , the RM model is formulated as:

$$\mathcal{G} : (P_{\text{BS}}, \hat{P}_{\text{raw}}) \rightarrow \{\boldsymbol{\mu}_n^{\text{rad}}\}_{n=1}^N. \quad (8)$$

The RM scheme will be elaborated in Section 3.2. Once the scatterer positions are identified, additional RadSplatter attributes are optimized to ensure accurate RSS predictions. The complete set of attributes and the rendering process will be discussed in Section 3.3.

### 3.2. Relaxed-Mean Reparameterization for Key Virtual Scatterers Positions Extraction

**Initial formulation:** Identifying key virtual scatterers in RM can be initially expressed as a geometric problem. The scatterer positions  $\{\boldsymbol{\mu}_n^{\text{rad}}\}_{n=1}^N$  should represent a subset of the raw point cloud  $\hat{P}_{\text{raw}}$ , while satisfying constraints that enforce proximity to the base station (BS) and reduce noise interference. Formally, this can be expressed as:

$$\text{Find } \{\boldsymbol{\mu}_n^{\text{rad}}\}_{n=1}^N \in \mathbb{R}^{N \times 3}, \quad (9a)$$

$$\text{s.t. } \hat{P}_N \subset \hat{P}_{\text{raw}}, \quad (9b)$$

$$\|\{\boldsymbol{\mu}_n^{\text{rad}}\}_{n=1}^N - \hat{P}_N\|_2 \leq \epsilon_1, \quad (9c)$$

$$\|\hat{P}_N - P_{\text{BS}}\|_2 \leq \epsilon_2. \quad (9d)$$

Here,  $\hat{P}_N$  is an intermediate subset of  $\hat{P}_{\text{raw}}$ , constraint (9b) ensures that the selected scatterers are derived from the original point cloud, preserving environmental features captured by the LiDAR sensor, constraint (9c) enforces that the final scatterer positions  $\{\boldsymbol{\mu}_n^{\text{rad}}\}_{n=1}^N$  remain close to  $\hat{P}_N$ , mitigating the impact of noise in the raw point cloud, and constraint (9d) prioritizes scatterers closer to the BS, as they contribute to dominant signal paths, such as line-of-sight (LoS) and strong non-line-of-sight (NLoS) reflections.

While this geometric formulation provides an intuitive starting point, it does not explicitly account for the relationship between scatterer positions and RSS predictions. The ultimate goal of RM is to identify scatterer positions  $\{\boldsymbol{\mu}_n^{\text{rad}}\}_{n=1}^N$  and other scatterer parameters that minimize the error in predicting RSS values at target locations. To optimize for RSS prediction, we reformulate the problem as minimizing a loss function  $\ell(\cdot, \cdot)$  between the predicted RSS  $\hat{y}_l$  and the ground truth RSS  $\mathbf{y}_l^{\text{GT}}$  collected at locations  $l \in \mathbb{L}_k$ :

$$\min_{\Phi_{\text{rad}}} \ell(\hat{y}_l, \mathbf{y}_l^{\text{GT}}), \quad \forall l \in \mathbb{L}_k, \quad (10)$$

where  $\hat{y}_l$  will be produced by the RadSplatter rendering representing by (7) with RadSplatter attributes  $\Phi_{\text{rad}}$  as will be illustrated in Section 3.3.

**Relaxed Reparameterization:** To enable efficient selection of scatterer positions, we reparameterize  $\boldsymbol{\mu}_n^{\text{rad}}$  using a trainable selection matrix  $\mathbf{T} \in \mathbb{R}^{N \times R}$  and bias term  $\mathbf{B} \in \mathbb{R}^{N \times 3}$  as:

$$\{\boldsymbol{\mu}_n^{\text{rad}}\}_{n=1}^N = \mathbf{T} \hat{P}_{\text{raw}} + \mathbf{B}, \quad (11)$$

where  $\mathbf{T}$  selects a subset of points from the raw point cloud  $\hat{P}_{\text{raw}}$ , and  $\mathbf{B}$  refines these positions to mitigate noise. The selection matrix  $\mathbf{T}$  is constrained to lie in the simplex space:

$$\mathbf{T} \in \mathbb{S} = \left\{ \mathbf{T} \in \mathbb{R}^{N \times R} \mid T_{n,r} \geq 0, \sum_{r=1}^R T_{n,r} = 1 \forall n \in [N] \right\}. \quad (12)$$

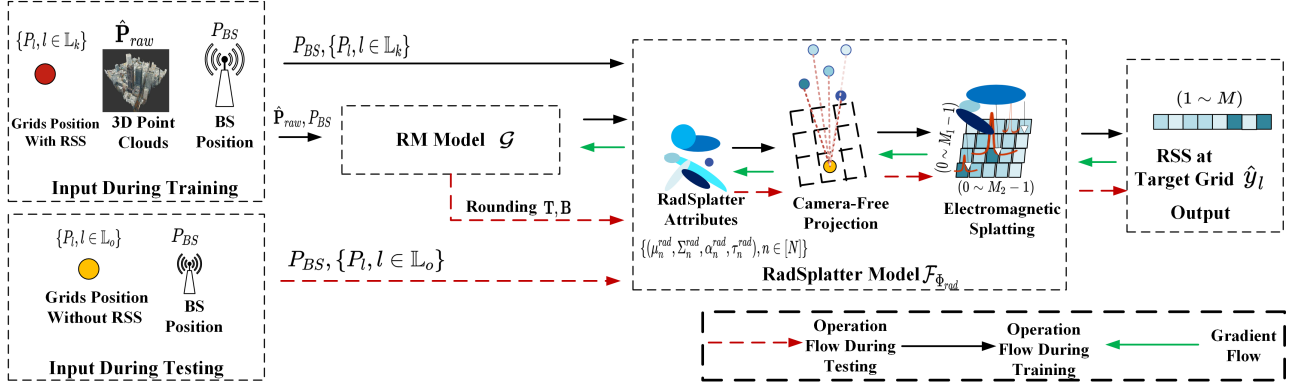


**Figure 3. An Overview of the RadSplatter Framework:** The raw 3D point clouds, often captured via LiDAR sensors, are efficiently denoised and scaled down by the optimization-based *RM* sub-model. This preprocessing model reparameterizes the means of key virtual scatterers for the RadSplatter framework. Once the scatterer positions are identified, additional signal-related RadSplatter attributes are optimized to ensure accurate RSS predictions. This design encodes virtual scatterers as a set of 3D Gaussians, each embedding attenuation and signal characteristics. To project these 3D Gaussian representations onto the *beamspace* for beam-wise RSSs, a novel *camera-free projection* technique is employed. Finally, the RSSs values at the target grid are rendered using the *electromagnetic splatting* method.

To ensure sparsity and distinctiveness, we enforce a Maximum Element Constraint (MEC), which requires the largest element in each row of  $\mathbf{T}$  to dominate:

$$\max_r \mathbf{T}_{n,r} \gg \mathbf{T}_{n,r'}, \quad \forall n \in [N], r' \neq \arg \max_r \mathbf{T}_{n,r}. \quad (13)$$

After reparameterization, the final optimization problem is

$$\min_{\mathbf{T}, \mathbf{B}, \Phi_{\text{rad}} \setminus \{\mu_n^{\text{rad}}\}_{n=1}^N} \ell(\hat{\mathbf{y}}_l, \mathbf{y}_l^{\text{GT}}) + \ell_{\text{reg}}, \quad (14a)$$

$$\text{s.t. } \{\mu_n^{\text{rad}}\}_{n=1}^N = \mathbf{T} \hat{\mathbf{P}}_{\text{raw}} + \mathbf{B}, \quad (14b)$$

$$\mathbf{T} \in \mathcal{S}. \quad (14c)$$

The regularization term  $\ell_{\text{reg}}$  enforces design principles such as proximity to the BS, noise mitigation, and sparsity in the selection matrix  $\mathbf{T}$  as

$$\ell_{\text{reg}} = \lambda_1 \|\mathbf{T} \hat{\mathbf{P}}_{\text{raw}} - P_{\text{BS}}\|_2 + \lambda_2 \|\mathbf{B}\|_2 + \lambda_{\text{MEC}} \|\mathbf{T} - 1\|_{\infty, 2} + \lambda_{\text{sparsity}} \|\mathbf{T}\|_1, \quad (15)$$

where the  $\ell_1$ -penalty and the MEC penalty ensure that each scatterer is associated with a small number of dominant points from the raw point cloud  $\hat{\mathbf{P}}_{\text{raw}}$ .

### 3.3. RadSplatter for RSS Synthesis

After efficiently extracting the positions,  $\{\mu_n^{\text{rad}}\}_{n=1}^N$  of key virtual scatterers through the RM reparameterization model (Section 3.2), the next step in RadSplatter is to determine the remaining properties of the major virtual scatterers to accurately synthesize RSS values. These properties, referred to as RadSplatter attributes, include attenuation signal  $\{\alpha_n^{\text{rad}}\}_{n=1}^N$ , RSS-encoded spherical harmonics coefficients  $\{\tau_n^{\text{rad}}\}_{n=1}^N$ , and the covariance matrices  $\{\Sigma_n^{\text{rad}}\}_{n=1}^N$ . These

attributes are optimized to align with the physical principles of wireless signal propagation, ensuring accurate RSS predictions.

**RadSplatter Attributes:** The signal attenuation  $\alpha_n^{\text{rad}}$  models attenuation strength factor caused by the scatterer's distance from the BS and corresponding phase shift. The direction vector from the BS to the  $n$ -th scatterer is defined as  $\mathbf{d}_n = P_{\text{BS}} - \mu_n^{\text{rad}}$ . To enhance spatial resolution, we encode the distance information using a position encoding function inspired by (Tancik et al., 2020)  $\gamma(\mathbf{d}_n) = [\sin(\pi \mathbf{d}_n), \dots, \sin(\pi^V \mathbf{d}_n), \cos(\pi^V \mathbf{d}_n)]$ , where  $V$  is the order of the encoding. A shallow multi-layer perceptron (MLP) is then applied to embed  $\gamma(\mathbf{d}_n)$  to derive the complex attenuation signal with phase shift  $\phi_n^{\text{rad}}$ :

$$\alpha_n^{\text{rad}} = \text{MLP}_1(\gamma(\mathbf{d}_n); \Phi_1) \odot e^{j\phi_n^{\text{rad}}}, \quad \forall n \in [N], \quad (16)$$

where  $\Phi_1$  represents the trainable parameters of the MLP. This formulation ensures that  $\alpha_n^{\text{rad}}$  accurately models the scatterer's attenuation effect.

To model view-dependent variations in RSS, we adapt SH functions, commonly used in visual tasks, to encode RSS *beamspace* information. Specifically, we introduce RSS-encoded SH coefficients  $\tau_n^{\text{rad}} \in \mathbb{R}^{M \times (k+1)^2}$ , where  $M = M_1 \times M_2$  is the total number of beams and  $k$  is the degree of the SH function. The covariance matrices  $\Sigma_n^{\text{rad}}$  define the anisotropic spatial uncertainty of each scatterer. We adopt a similar parameterization as that in 3DGS for vision tasks (Zhou et al., 2024a; Cheng et al., 2024).

With the RadSplatter attributes  $\mu_n^{\text{rad}}$ ,  $\Sigma_n^{\text{rad}}$ ,  $\alpha_n^{\text{rad}}$ , and  $\tau_n^{\text{rad}}$  defined, the next step in RadSplatter is the rendering process, which involves a camera-free projection of the scatterers

onto the *beamspace* and synthesizing the beam-wise RSS values by *electromagnetic splatting*.

**Camera-free Projection:** A novel *camera-free projection approach* is proposed to map the 3D virtual scatterers onto the 2D plane of *beamspace*, as discussed in Section 2.2. Unlike traditional 3D Gaussian splatting, which computes color values for pixels, Radsplatter aggregates contributions of scatterers to synthesize beam-wise RSS values. There are several key differences compared with the camera model in the optical 3DGS-based model: First, there are no intrinsic or extrinsic camera parameters. Second, no exact projection formula exists for mapping spatial 3D to the 2D beam-wise RSS *beamspace*. To address this, we introduce two encoded-decoded structured MLPs for a camera-free projection that recovers the 2D Gaussian representation: the means  $\mathbf{x} \in \mathbb{R}^2$  and precision, w.r.t. the inverse of variance,  $\mathbf{\Lambda}_n \in \mathbb{R}^{2 \times 2}$ :

$$\begin{aligned} \mathbf{x}_n &= \text{MLP}_2(\boldsymbol{\mu}_n^{\text{rad}}; \Phi_2) \odot \mathbf{o}, \quad \forall n \in [N], \\ \mathbf{\Lambda}_n &= \text{MLP}_3(\boldsymbol{\Sigma}_n^{\text{rad}}; \Phi_3), \quad \forall n \in [N], \end{aligned} \quad (17)$$

where  $\Phi_2$  and  $\Phi_3$  are the trainable parameters of the means-projection and precision-projection functions. Here,  $\mathbf{o} = [M_1 - 1, M_2 - 1]$  is a vector. The activation function of the last layer in the means-projection function  $\text{MLP}_2(\cdot; \Phi_2)$  is set as a Sigmoid function to constrain the  $\mathbf{x}_n$  remains within the  $M_1 \times M_2$  beam-wise RSS *beamspace*, as shown in the top right corner of Figure 1. To compute  $\mathbf{w}_n \in \mathbb{R}^{M_1 \times M_2}$  of the 2D Gaussian splats over the beam-wise RSS *beamspace*, given the precision and means from Eq. (17), the sampled indices of the *beamspace*  $\mathbf{m}(m_1, m_2) = [m_1 - 1, m_2 - 1] \in \mathbb{R}^2, \forall m_1 \in [M_1], \forall m_2 \in [M_2]$  can be used:

$$\mathbf{w}_n(m_1, m_2) = \exp\left(-\frac{t}{2} \mathbf{g}_n(m_1, m_2)^T \mathbf{\Lambda}_n \mathbf{g}_n(m_1, m_2)\right), \quad (18)$$

where  $\mathbf{g}_n(m_1, m_2) = \mathbf{m}(m_1, m_2) - \mathbf{x}_n, \forall m_1 \in [M_1], \forall m_2 \in [M_2]$  and  $t$  is a scaling constant.

**Electromagnetic Splatting:** After the camera-free coordinate projection transformation, during rendering, each 2D Gaussian contributes to multiple RSS beams. Specifically, the depth ordering of the 3D Gaussian means,  $\boldsymbol{\mu}_n^{\text{rad}}, n \in [N]$ , relative to the target grid  $P_l$ , determines their contribution. These 2D Gaussians are sorted by ascending depth order. This sorting is represented by the permutation operation  $\pi : \boldsymbol{\mu} \rightarrow \Pi \boldsymbol{\mu}$ , where  $\Pi$  is a meaningful permutation matrix denoting the sorting operation as a one-to-one mapping  $n \rightarrow \pi(n), n \in [N]$ . The value of each RSS beam is the cumulative contribution of all sorted 2D Gaussians, as illustrated in the *electromagnetic splatting module* in Figure 3. To reconstruct the beam-wise RSS for the target grid, and following Eq. (5), the *electromagnetic splatting module* integrates the attributes of the  $n$ -th scatterer as:

$$\Delta \hat{\boldsymbol{\beta}}_n \odot e^{j \Delta \hat{\varphi}_n} = \mathbf{c}_{\pi(n)}^{\text{rad}} \odot \boldsymbol{\alpha}_{\pi(n)}^{\text{att}} \odot \text{vec}(\mathbf{w}_{\pi(n)}), \quad (19)$$

where  $\text{vec}(\cdot)$  denotes the matrix vectorization operation, and  $\mathbf{c}_{\pi(n)}^{\text{rad}} \in \mathbb{C}^M$  represents the view-dependent radio signal in beamspace:

$$\mathbf{c}_{\pi(n)}^{\text{rad}} = \mathbf{s} \mathbf{h}(\boldsymbol{\tau}_{\pi(n)}^{\text{rad}}, \mathbf{v}_{\pi(n)}^{\text{rad}}, k) \odot e^{j \varphi_{\pi(n)}^{\text{rad}}}, \quad \forall n \in [N], \quad (20)$$

where the view direction is  $\mathbf{v}_{\pi(n)}^{\text{rad}} = \frac{P_l - \boldsymbol{\mu}_{\pi(n)}^{\text{rad}}}{|P_l - \boldsymbol{\mu}_{\pi(n)}^{\text{rad}}|_2}$ , and  $\varphi_{\pi(n)}^{\text{rad}} \in \mathbb{R}^M$  denotes the signal phase. The final attenuation signal  $\boldsymbol{\alpha}_{\pi(n)}^{\text{att}}$  accounts for the accumulated attenuation effects on the  $\pi(n)$ -th scatterer, expressed as:

$$\boldsymbol{\alpha}_{\pi(n)}^{\text{att}} = \hat{\boldsymbol{\alpha}}_n^{\text{rad}} \odot \prod_{i=1}^{n-1} (1 - \hat{\boldsymbol{\alpha}}_i^{\text{rad}}) \in \mathbb{C}^M, \quad (21)$$

with the sorted attenuation signal  $\hat{\boldsymbol{\alpha}}_n^{\text{rad}} = \boldsymbol{\alpha}_{\pi(n)}^{\text{rad}}, \forall n \in [N]$ . These formulations assume that each scatterer acts as a virtual transmitter, retransmitting a new complex signal modified by an accumulated complex attenuation factor. Using the RSS-related Eq. (4), the final blended RSS  $\hat{\mathbf{y}}_l$  is computed as:

$$\hat{\mathbf{y}}_l = P \left| \sum_{n=1}^N \Delta \hat{\boldsymbol{\beta}}_n \odot e^{j \Delta \hat{\varphi}_n} \right|^2, \quad (22)$$

where the transmit power  $P$  is usually known in advance.

### 3.4. Optimizing RadSplatter

Summarizing Sections 3.2 and 3.3, the trainable parameters of RadSplatter are from the reparameterization of RadSplatter attributes, the camera-free projection, and the electromagnetic splatting listed as

$$\mathbf{\Gamma}_{\text{rad}} = \{\mathbf{T}, \mathbf{B}, \Phi_1, \Phi_2, \Phi_3, \{\boldsymbol{\tau}_n^{\text{rad}}, \boldsymbol{\Sigma}_n^{\text{rad}}, \boldsymbol{\phi}_n^{\text{rad}}, \boldsymbol{\varphi}_n^{\text{rad}}\}_{n=1}^N\}.$$

Combining with the optimization formulation of  $\mathbf{T}$  and  $\mathbf{B}$  in (14), we train the RadSplatter models using the following loss with mini-batch gradient descent:

$$\ell_{\text{final}}(\mathbf{\Gamma}_{\text{rad}}) = \ell(\hat{\mathbf{y}}_l, \mathbf{y}_l^{\text{GT}}) + \ell_{\text{reg}}, \quad (23)$$

where  $\ell$  is a composite loss combining mean squared error (MSE) and total variation (TV) losses:

$$\ell = \underbrace{\frac{1}{|\mathbb{D}|} \sum_{l \in \mathbb{D}} (\hat{\mathbf{y}}_l - \mathbf{y}_l^{\text{GT}})^2}_{\text{MSE Loss}} + \lambda_{\text{TV}} \cdot \underbrace{\frac{1}{|\mathbb{D}|} \sum_{l \in \mathbb{D}} \|\hat{\mathbf{y}}_l - \hat{\mathbf{y}}_{\text{KNN}(l)}\|_1}_{\text{TV Loss}}. \quad (24)$$

Here,  $\lambda_{\text{TV}}$  controls the TV loss weight,  $\mathbb{D}$  is the mini-batch sample set with  $|\mathbb{D}|$  samples,  $\mathbf{y}_{\text{KNN}(l)}$  denotes the prediction for the nearest neighbor of the  $l$ -th sample in grid positions within  $\mathbb{D}$ . By balancing accuracy, smoothness, and regularization, the ternary final area-by-area loss (23) provides a

robust framework for RSS radiomap extrapolation, ensuring precise and spatially coherent predictions.

Given training set grids  $\mathbb{L}_k$  and testing set grids  $\mathbb{L}_o$ , in addition to the design of the loss function, a novel training scheme, termed the recursive fine-tuning scheme, is proposed to further enhance performance. Observing that data points within the grids  $\mathbb{L}_o$  closer to the boundary, which separates the grids  $\mathbb{L}_k$  and the grids  $\mathbb{L}_o$ , are easier to recover, this scheme leverages the nature of the extrapolation task within spatial data to progressively recover data near the boundary  $\mathbb{L}_D$ . The recursive fine-tuning scheme for outdoor scenes consists of three key steps:

- **Step 1. Training on the Existing Training Set:** Train the RadSplatter model by minimizing the final loss function (23) on grids  $\mathbb{L}_k$ , where RSS is assumed known, for predefined  $K$  iterations.
- **Step 2. Predicting RSS Near the Boundary:** Identify grids  $\mathbb{L}_D$  within  $D$  units of distance near boundaries from  $\mathbb{L}_o$ , and predict the RSSs at these grids using the trained RadSplatter model by step 1.
- **Step 3. Constructing a New Training and Testing Set:** Incorporate the predicted RSS values and their corresponding grids  $\mathbb{L}_D$  into the existing training set  $\mathbb{L}_k$  and remove them from the testing set  $\mathbb{L}_o$ :  $\mathbb{L}_k = \{l | l \in \mathbb{L}_k \cup \mathbb{L}_D\}$ ,  $\mathbb{L}_o = \{l | l \in \mathbb{L}_o \setminus \mathbb{L}_D\}$ .

These three steps are repeated iteratively until the RSS values for all grids in  $\mathbb{L}_o$  are covered by  $\mathbb{L}_k$ . Then, the RadSplatter model with trained parameters is selected as the final model to evaluate on the original testing set  $\mathbb{L}_o$ . Specifically, in the *testing phase*, instead of directly using  $\mathbf{T}$  produced in the *training phase*, we round it by selecting the maximum element in each row and setting other elements to zero, ensuring the rounded  $\mathbf{T}$  being binary selection matrix  $\mathbf{T} \in \mathbb{B}^{N \times R}$ , where  $\sum_{r=1}^R \mathbf{T}_{n,r} = 1, \forall n \in [N]$ . Then we use  $\{\mu_n^{rad}\}_{n=0}^{N-1}$  determined by these for RadSplatter.

## 4. Synthetic Data Evaluation

To better understand the performance of RadSplatter in representing virtual scatters with several key radio-related attributes versus its performance in extrapolating RSS radiomap in unseen locations, we first evaluate the RadSplatter relying on a limited, sparse set of measurements on synthetic datasets.

**Synthetic Datasets:** We use the synthetic data sets based on Shanghai City with total 5,963,068 point clouds captured by LiDAR sensor to describing the outdoor complex environment. Figure 2 shows the layout geometry of the outdoor environment, whose size is around  $1000 \times 1200 \times 110.5m^3$ , and the spatial distribution of collected outdoor data from

central 6,310 grids (each of  $10 \times 10m^2$ ), all of which are measured at the same height  $1m$  by ray tracing techniques (Luo et al., 2023). Note that there is only one main BS in this unit coverage area. To emulate the signal interference encountered in real-world scenarios, we incorporate 3 dB noise into the data. Moreover, we separate the total measurements into training set with  $|\mathbb{L}_k| = 5,566$  red grids and testing set with only  $|\mathbb{L}_o| = 744$  yellow grids to evaluate RadSplatter.

### 4.1. RSS Radiomap Extrapolation Results

We first evaluate how efficiently and accurately our proposed RadSplatter can predict RSS compared to three baselines on the inference cost time<sup>3</sup> and the metric Mean Absolute Error (MAE), whose lower values indicate greater similarity between predicted and ground truth samples, defined as:

$$MAE = \frac{1}{|\mathbb{L}_o|} \sum_{l \in \mathbb{L}_o} |\hat{y}_l - y_l^{GT}|, \quad (25)$$

where  $|\mathbb{L}_o|$  is the total number of grids in the test dataset and  $\hat{y}_l$  denotes the predicted RSS from different models:

- **Kriging Method:** This approach is the typical model-based method for spatial data, which is also beneficial for radiomap-related interpolation tasks.
- **Variational Autoencoder (VAE):** VAE is commonly used to generate new data samples by mapping observed data to a continuous latent space. Here, we use VAE to predict the spatial RSSs at target grids.
- **NeRF<sup>2</sup>:** NeRF<sup>2</sup> is a SOTA learning-based method for spatial spectrum synthesis using the NeRF technique. After training, NeRF<sup>2</sup> can predict the spatial RSSs at arbitrary target grids' positions.

Table 1. Performance Comparison on Synthetic Dataset

Method	MAE (dB)	Inference Time (s)
Kriging	11.307	0.010
VAE	10.306	0.007
NeRF <sup>2</sup>	9.867	0.020
RadSplatter	7.564	0.004

Table 1 compares MAE metric values and inference time costs for test set measurements among the proposed RadSplatter and other baselines. Our model's predictions align best with the ground truth, achieving an MAE of less than 8 dB. RadSplatter outperforms all baselines with a 7.564 dB MAE, while others exceed 9 dB. The slightly inferior performance of NeRF<sup>2</sup> is due to challenges in locating the spatial positions of virtual scatterers along propagation paths

<sup>3</sup>All experiments are carried out on NVIDIA A30.

without using any environmental features. Inference time cost refers to the average duration for a model to complete one inference cycle on a test data point. Results also show the rendering time required to synthesize one RSS at a target grid. RadSplatter processes a single sample in  $0.004s$ , while NeRF<sup>2</sup> takes  $0.02s$ , almost five-fold time. RadSplatter demonstrates superior computational efficiency, suitable for latency-sensitive applications, whereas the NeRF-based model faces time complexity challenges due to the need to search the whole angular space before rendering.

#### 4.2. Impact of Extracted Virtual Scatterers

To further investigate the impact of extracted virtual scatterers on the RSS extrapolation task, we conduct additional ablation experiments with three baselines, all of which are variants of RadSplatter: 1) In the *Random-Points-Opt* model,  $N$  points are randomly sampled from the  $R$  raw point clouds  $\hat{P}_{raw}$  using the farthest point sampling method (Moening & Dodgson, 2003). These sampled points serve as the initial means of the key virtual scatterers  $\{\mu_n^{rad}\}_{n=1}^N$ , instead of employing the RM model to reparameterize them as in RadSplatter. Notably, the means  $\{\mu_n^{rad}\}_{n=1}^N$  in *Random-Points-Opt* are directly optimized during training alongside other parameters  $\Phi_{rad} \setminus \{\mu_n^{rad}\}_{n=1}^N$ . 2) Different from the *Random-Points-Opt* model, the *Random-Initial-Opt* model initializes the means of key virtual scatters  $\{\mu_n^{rad}\}_{n=1}^N$  from a uniform distribution within the coverage area without using raw point cloud data  $\hat{P}_{raw}$ . 3) The *Random-Initial-Fixed* model follows the same initialization as *Random-Initial-Opt* for the means  $\{\mu_n^{rad}\}_{n=1}^N$  of key virtual scatterers. However, unlike in *Random-Initial-Opt*, these means remain fixed during training, and only the other parameters  $\Phi_{rad} \setminus \{\mu_n^{rad}\}_{n=1}^N$  are optimized.

Table 2. Performance Comparison of Ablation Experiments

Method	MAE (dB)
RadSplatter	7.564
Random-Points-Opt	8.167
Random-Initial-Opt	10.463
Random-Initial-Fixed	53.234

The performance results are summarized in Table 2, leading to three key conclusions: 1) Comparing *Random-Initial-Fixed* and *Random-Initial-Opt* highlights the necessity of optimizing the means of key virtual scatterers  $\{\mu_n^{rad}\}_{n=1}^N$  in the RadSplatter model to enhance its expressiveness, demonstrating the importance of introducing bias  $\mathbf{B}$  to add flexibility. 2) Comparing *Random-Points-Opt* and *Random-Initial-Opt* confirms that point cloud modality data significantly improve the RSS radiomap extrapolation task. 3) Comparing *RadSplatter* and *Random-Points-Opt* demonstrates that raw point clouds  $\hat{P}_{raw}$ , despite their noise, can effectively guide the selection of means of key virtual scatterers

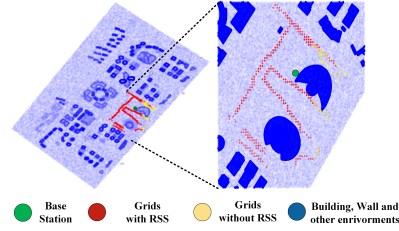


Figure 4. Illustration of Hangzhou City 3D Outdoor Environment.

via the novel and efficient RM reparameterization model, outperforming random selection methods.

### 5. Real-world Data Evaluation

As a supplementary evaluation, we have collected real RSSs data and point cloud data in Hangzhou City. Our proposed model has been evaluated on this dataset to demonstrate its practical applicability and performance.

**Real-world Datasets:** The real-world datasets are collected from Hangzhou City, consisting of 8,711,005 LiDAR-captured point clouds to model obstacles, as shown in the zoomed view in Figure 4. RSSs data are collected from 492 grids ( $10 \times 10 m^2$ ) within an area containing a single main BS. Then the dataset is divided into  $|\mathbb{L}_k| = 417$  red grids for training and  $|\mathbb{L}_o| = 75$  yellow grids for testing.

Table 3. Performance Comparison on Real-world Dataset

Method	MAE (dB)	Inference Time (s)
Kridging	9.656	0.183
VAE	8.728	0.011
NeRF <sup>2</sup>	7.313	0.585
RadSplatter	7.035	0.018

Table 3 presents the prediction performance and computational efficiency of the RadSplatter framework for the real-world outdoor RSS radiomap extrapolation task. The results clearly demonstrate that the proposed RadSplatter framework outperforms other baseline methods while maintaining substantial computational efficiency, making it highly suitable for practical applications.

### 6. Conclusion

In this work, we first extended 3DGS to the radio frequency domain, leveraging camera-free RadSplatter to extrapolate RSSs with high accuracy from sparse measurements in outdoor environment. By efficiently selecting the means of key virtual scatterers from dense point clouds aided by RM parameterization model, the model captured intricate multipath propagation characteristics. Experiments and analysis validated the effectiveness of these scatterers, advancing the state-of-the-art in wireless network modeling and ex-

trapolation performance and highlighting the transformative potential of integrating advanced 3D modeling techniques with wireless propagation analysis for next-generation applications in the radio domain.

## References

- Bertoni, H. L. *Radio propagation for modern wireless systems*. Pearson Education, 1999.
- Bi, S., Lyu, J., Ding, Z., and Zhang, R. Engineering radio maps for wireless resource management. *IEEE Wireless Commun.*, 26(2):133–141, 2019.
- Cheng, K., Long, X., Yang, K., Yao, Y., Yin, W., Ma, Y., Wang, W., and Chen, X. Gaussianpro: 3d gaussian splatting with progressive propagation. In *Forty-first International Conference on Machine Learning*, 2024.
- Demarsin, K., Vanderstraeten, D., Volodine, T., and Roose, D. Detection of closed sharp edges in point clouds using normal estimation and graph theory. *Computer-Aided Design*, 39(4):276–283, 2007.
- Fridovich-Keil, S., Yu, A., Tancik, M., Chen, Q., Recht, B., and Kanazawa, A. Plenoxels: Radiance fields without neural networks. In *Proceedings of the IEEE/CVF conference on computer vision and pattern recognition*, pp. 5501–5510, 2022.
- Fu, Y., Wang, X., Liu, S., Kulkarni, A., Kautz, J., and Efros, A. A. Colmap-free 3d gaussian splatting. In *2024 IEEE/CVF Conference on Computer Vision and Pattern Recognition (CVPR)*, pp. 20796–20805, 2024. doi: 10.1109/CVPR52733.2024.01965.
- Kapusuz, K. Y. and Kara, A. Determination of scattering center of multipath signals using geometric optics and fresnel zone concepts. *Engineering Science and Technology, an International Journal*, 17(2):50–57, 2014.
- Kerbl, B., Kopanas, G., Leimkühler, T., and Drettakis, G. 3d gaussian splatting for real-time radiance field rendering. *ACM Trans. Graph.*, 42(4):139–1, 2023.
- Kingma, D. P. Adam: A method for stochastic optimization. *arXiv preprint arXiv:1412.6980*, 2014.
- Kuo, S.-P. and Tseng, Y.-C. Discriminant minimization search for large-scale rf-based localization systems. *IEEE Transactions on Mobile Computing*, 10(2):291–304, 2010.
- Li, J., Zhang, J., Bai, X., Zheng, J., Ning, X., Zhou, J., and Gu, L. Dngaussian: Optimizing sparse-view 3d gaussian radiance fields with global-local depth normalization. In *Proceedings of the IEEE/CVF Conference on Computer Vision and Pattern Recognition*, pp. 20775–20785, 2024.
- Lu, H., Vatheuer, C., Mirzasoleiman, B., and Abari, O. Newrf: A deep learning framework for wireless radiation field reconstruction and channel prediction. In *Forty-first International Conference on Machine Learning*, 2024.
- Luo, Z.-Q., Zheng, X., López-Pérez, D., Yan, Q., Chen, X., Wang, N., Shi, Q., Chang, T.-H., and Garcia-Rodriguez, A. SRCON: A data-driven network performance simulator for real-world wireless networks. *IEEE Commun. Mag.*, 61(6):96–102, Jun. 2023. doi: 10.1109/MCOM.001.2200179.
- Mi, H., Ai, B., He, R., Bodi, A., Caromi, R., Wang, J., Senic, J., Gentile, C., and Miao, Y. Measurement-based prediction of mmwave channel parameters using deep learning and point cloud. *IEEE Open Journal of Vehicular Technology*, 2024.
- Mildenhall, B., Srinivasan, P. P., Tancik, M., Barron, J. T., Ramamoorthi, R., and Ng, R. Nerf: Representing scenes as neural radiance fields for view synthesis. *Communications of the ACM*, 65(1):99–106, 2021.
- Moening, C. and Dodgson, N. A. Fast marching farthest point sampling. Technical report, University of Cambridge, Computer Laboratory, 2003.
- Qi, C. R., Yi, L., Su, H., and Guibas, L. J. Pointnet++: Deep hierarchical feature learning on point sets in a metric space. *Advances in neural information processing systems*, 30, 2017.
- Radford, A. Unsupervised representation learning with deep convolutional generative adversarial networks. *arXiv preprint arXiv:1511.06434*, 2015.
- Rusu, R. B. and Cousins, S. 3d is here: Point cloud library (pcl). In *2011 IEEE international conference on robotics and automation*, pp. 1–4. IEEE, 2011.
- Sato, K., Inage, K., and Fujii, T. Radio environment map construction with joint space-frequency interpolation. In *2020 International Conference on Artificial Intelligence in Information and Communication (ICAIIIC)*, pp. 051–054. IEEE, 2020.
- Sun, Y., Zhang, J., Yu, L., Zhang, Z., and Zhang, P. How to define the propagation environment semantics and its application in scatterer-based beam prediction. *IEEE Wireless Communications Letters*, 12(4):649–653, 2023.
- Tancik, M., Srinivasan, P., Mildenhall, B., Fridovich-Keil, S., Raghavan, N., Singhal, U., Ramamoorthi, R., Barron, J., and Ng, R. Fourier features let networks learn high frequency functions in low dimensional domains. *Advances in neural information processing systems*, 33:7537–7547, 2020.

- Teganya, Y. and Romero, D. Deep completion autoencoders for radio map estimation. *IEEE Transactions on Wireless Communications*, 21(3):1710–1724, 2021.
- Villani, V., Pini, F., Leali, F., and Secchi, C. Survey on human–robot collaboration in industrial settings: Safety, intuitive interfaces and applications. *Mechatronics*, 55: 248–266, 2018.
- Zhao, X., An, Z., Pan, Q., and Yang, L. Nerf2: Neural radio-frequency radiance fields. In *Proceedings of the 29th Annual International Conference on Mobile Computing and Networking*, pp. 1–15, 2023.
- Zhou, S., Chang, H., Jiang, S., Fan, Z., Zhu, Z., Xu, D., Chari, P., You, S., Wang, Z., and Kadambi, A. Feature 3dgs: Supercharging 3d gaussian splatting to enable distilled feature fields. In *Proceedings of the IEEE/CVF Conference on Computer Vision and Pattern Recognition*, pp. 21676–21685, 2024a.
- Zhou, X., Lin, Z., Shan, X., Wang, Y., Sun, D., and Yang, M.-H. Drivinggaussian: Composite gaussian splatting for surrounding dynamic autonomous driving scenes. In *Proceedings of the IEEE/CVF Conference on Computer Vision and Pattern Recognition*, pp. 21634–21643, 2024b.
- Zwicker, M., Pfister, H., Van Baar, J., and Gross, M. Ewa splatting. *IEEE Transactions on Visualization and Computer Graphics*, 8(3):223–238, 2002.

## A. Details of Implementations

We implement RadSplatter in Pytorch. To process dense point clouds, we first extract edge points, which are typically defined by significant changes in surface normal vectors (Demarsin et al., 2007), such as boundaries of obstacles or regions with differing properties, and are more likely to represent virtual scatterers. Accurately identifying these edge points enhances model quality and reduces time costs. This results in a subset of points, maintaining the structural integrity of the original cloud (Qi et al., 2017). The RadSplatter, with  $N = 2,000$  points, can be trained using the Adam optimizer (Kingma, 2014) and the area-by-area loss function in Eq. (23). For NeRF<sup>2</sup>, we adapt the open-source code (Zhao et al., 2023) to our RSS radiomap extrapolation task. All baselines are retrained on our datasets and evaluated on the same test sets.

## B. Visualization of Extracted Virtual Scatterers

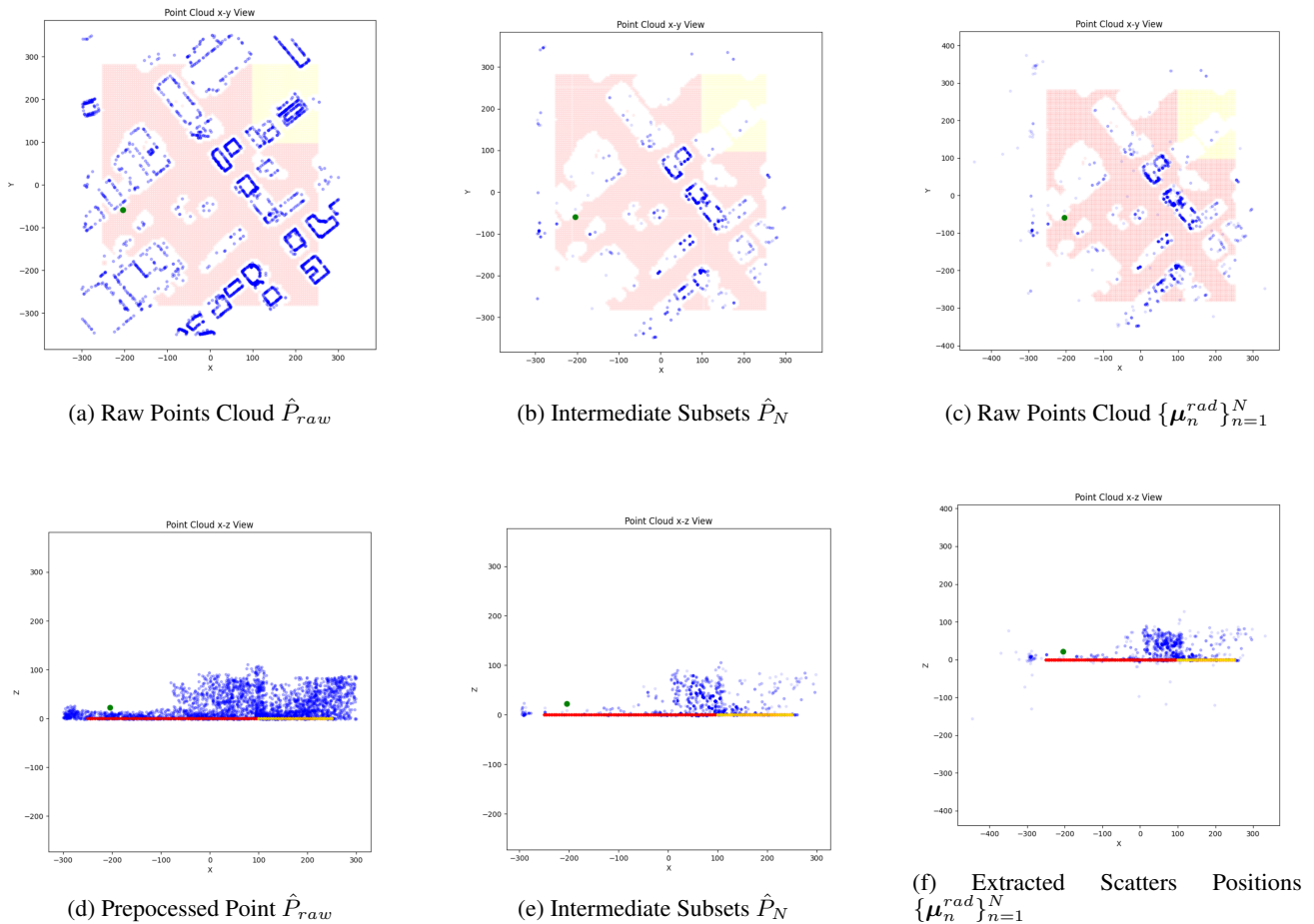


Figure 5. Visualization of Extracted Results: (a)-(c) Top View of Prediction results for the three phases of extracting, (d)-(f) Front View of Prediction results for the three phases of extracting.

In particular, with the aid of point cloud modality data and the white-block RM reparameterization model discussed in Section 3.2, the proposed RadSplatter model can represent virtual scatterers and render the targeted RSS in out-of-boundary areas using camera-free projection and electromagnetic splatting. Figure 5 visualizes the three phases of extracting virtual scatterers position: raw points cloud  $\hat{P}_{raw}$ , intermediate subsets  $\hat{P}_N$ , and extracted virtual scatterers position on the Shanghai City synthetic datasets.